Received: 22 September 2021 | Revised: 20 October 2021 | Accepted: 20 October 2021

DOI: 10.1002/cey2.171

RESEARCH ARTICLE

CARBON ENERGY WILEY

Tailoring structural properties of carbon via implanting optimal co nanoparticles in n-rich carbon cages toward high-efficiency oxygen electrocatalysis for rechargeable zn-air batteries

Jie Yu[1] | **Yawen Dai**[1] | **Zhenbao Zhang**[1] | **Tong Liu**[1] | **Siyuan Zhao**[1] | **Chun Cheng**[1] | **Peng Tan**[2] | **Zongping Shao**[3,4] | **Meng Ni**[1]

[1]Department of Building and Real Estate, The Hong Kong Polytechnic University, Kowloon, Hong Kong, China

[2]Department of Thermal Science and Energy Engineering, University of Science and Technology of China, Hefei, Anhui, China

[3]State Key Laboratory of Materials-Oriented Chemical Engineering, Department of Chemical Engineering, College of Chemical Engineering, Nanjing Tech University, Nanjing, China

[4]Department of Chemical Engineering, Curtin University, Perth, Western Australia, Australia

Correspondence

Meng Ni, Department of Bldg and Real Estate, Research Institute for Sustainable Urban Development (RISUD) & Research Institute for Smart Energy (RISE), The Hong Kong Polytechnic University, Hung Hom, Kowloon, 999077 Hong Kong, China.
Email: meng.ni@polyu.edu.hk

Zongping Shao, State Key Laboratory of Materials-Oriented Chemical Engineering, Department of Chemical Engineering, College of Chemical Engineering, Nanjing Tech University, No. 30 PuZhu South Rd., 211800 Nanjing, China.
Email: shaozp@njtech.edu.cn

Abstract

Rational construction of carbon-based materials with high-efficiency bifunctionality and low cost as the substitute of precious metal catalyst shows a highly practical value for rechargeable Zn-air batteries (ZABs) yet it still remains challenging. Herein, this study employs a simple mixing-calcination strategy to fabricate a high-performance bifunctional composite catalyst composed of N-doped graphitic carbon encapsulating Co nanoparticles (Co@NrC). Benefiting from the core-shell architectural and compositional advantages of favorable electronic configuration, more exposed active sites, sufficient electric conductivity, rich defects, and excellent charge transport, the optimal Co@NrC hybrid (Co@NrC-0.3) presents outstanding catalytic activity and stability toward oxygen-related electrochemical reactions (oxygen reduction and evolution reactions, i.e., ORR and OER), with a low potential gap of 0.766 V. Besides, the rechargeable liquid ZAB assembled with this hybrid electrocatalyst delivers a high peak power density of 168 mW cm^{-2}, a small initial discharge-charge potential gap of 0.45 V at 10 mA cm^{-2}, and a good rate performance. Furthermore, a relatively large power density of 108 mW cm^{-2} is also obtained with the Co@NrC-0.3-based flexible solid-state ZAB, which can well power LED lights. Such work offers insights in developing excellent bifunctional electrocatalysts for both OER and ORR and highlights their potential applications in metal-air batteries and other energy-conversion/storage devices.

KEYWORDS

Co nanoparticles, core-shell nanostructure, N-doped graphitic carbon, oxygen electrocatalysis, Zn-air battery

Jie Yu and Yawen Dai equally contributed to this study.

1 | INTRODUCTION

The limited resources of traditional fossil fuels on Earth and the severe environmental issues from their overconsumption have prompted considerable research activities on various clean and sustainable energy storage and conversion systems.[1,2] Previously, lithium-ion batteries were considered as the advanced electrochemical energy storage device, however, due to the scarcity of lithium resources, the safety concern about the organic liquid electrolyte, and the limited energy density, which may not be suitable for larger-scale use in the future.[3] One better choice is rechargeable zinc-air batteries (ZABs), which use metallic zinc as anode and oxygen from the air as the cathodic reactant and have received intensive attention recently. The advantageous features of ZABs for electrochemical energy storage include high theoretical energy density (1218 Wh kg^{-1}), an abundance of raw materials (Zn), low cost (more than 6-fold lower price for Zn than for Li), and high safety (with an aqueous alkaline solution as the electrolyte).[4–6] Nevertheless, in such devices, the main challenge for ZABs relies on the development of air electrode catalysts with superior bifunctionality, that is, high activity for both oxygen reduction and evolution reactions (ORR and OER), which determines the round-trip efficiency. By far, the best-performing ORR electrocatalysts still mainly focus on Pt-based materials, and Ru- and Ir-based nanomaterials are perceived as the benchmark catalysts toward OER.[7–9] However, for these noble materials, not only the high price and scarcity become the short-slab of their widespread commercialization, but also their poor stability and insufficient catalytic bifunctionality are the highly significant concerns.[10,11] Therefore, high-efficiency and robust noble-metal-free bifunctional oxygen electrocatalysts are urgently required to satisfy the needs of the rechargeable ZABs.

Metal-free carbon materials show some outstanding properties, such as the low cost, earth abundance, superior conductivity, controllable surface chemistry, modified electronic structure, and so forth, which have provoked substantial attention in the electrocatalysis field, especially ORR.[12–17] Wei et al.[15] developed nitrogen-doped carbon nanosheets with size-defined mesopores by different SiO_2 templates as highly efficient metal-free catalyst for the ORR. When operating in alkaline media, the largest pore size of about 22 nm exhibits the highest ORR performance and the onset potential is only −0.01 V versus Ag/AgCl, which was attributed to the enhanced contact between electrolyte and reactants.[15] Sun et al.[16] demonstrated that a hybrid of an ultrathin N-doped holey carbon layer (HCL) and a graphene sheet overcome the drawbacks of holey graphene approaches and exhibit an impressive ORR activity with the onset potential of 1.0 V versus RHE. Previously, our group also fabricated three-dimensional hierarchical porous graphite carbon with rich defects as super ORR catalyst, which became the best one among all reported metal-free ORR catalysts so far. Although this common metal-free carbon delivered excellent ORR activity, its OER behavior was far from satisfied.[17] Only a few reports on carbon materials as super OER electrocatalysts were given.[18–20]

Heteroatom N introduction is regarded as a powerful strategy to ameliorate the catalytic activity of these carbon-based electrocatalysts.[21,22] The N dopants can well break the electroneutrality of the nearby carbon atoms, thus induce asymmetry of the charge distribution, bring about defects in neighboring sites, and thereby create positively charged sites in favor of O-related intermediates adsorption and reaction.[23,24] Nevertheless, as compared to the ORR, the space to enhance the OER activity is still rather limited. As a successful strategy, Deng et al.[25] reported a unique core-shell nanostructure in which transition-metal nanoparticles were encapsulated in a carbon layer, which displayed remarkable OER performance. In such a structure, the presence of metal nanoparticles can promote electron transfer from the inner metal core to the outer carbon layer, and thus the carbon shell became highly active with the accelerated O_2 adsorption and dissociation abilities; consequently, both OER and ORR behavior were well initiated.[26] In addition, the inner metal core was efficiently protected by the stable carbon shells from the harsh reaction condition.[26] More importantly, the enhanced catalytic properties related to the transferred charge are tightly associated with the corresponding metal proportion in the hybrids. Considering these points, in this study, we prepared a bifunctional catalytic material with a core-shell nanostructure consisting of Co nanoparticles encased by N-rich and graphitic carbon framework, through a simple and scalable one-step annealing route (Co@NrC). We probed the effect of Co amount on carbon structural properties and the resulting catalytic behavior. The optimal Co@NrC (Co@NrC-0.3) delivered remarkable electrocatalytic activities for ORR and OER under alkaline conditions, which only needed the potential gap (ΔE) of 0.766 V, as well as good durability. This result could totally be comparable with that of the commercial Pt/C and RuO_2 benchmarks. When served as the cathode electrocatalysts in practical rechargeable aqueous and all solid-state ZABs, the large peak power density, small charge-discharge polarization potential difference, and prolonged cycling lifespan were also offered for the Co@NrC-0.3 sample, showing a great potential of practical application.

2 | RESULTS AND DISCUSSIONS

The general fabrication procedure of the Co@NrC samples is illustrated in Scheme 1, which briefly was based on a facile premixing process with subsequently programmed carbonation (the details can be seen from the Supporting Information experimental section). The products prepared with different amounts of cobalt nitrate were denoted as Co@NrC-x ($x = 0.15$, 0.3, 0.45, or 0.6). According to the scanning electron microscopy (SEM) results, all as-prepared Co@NrC materials embraced a micron-sized interconnected flake-like morphology, and with an increase in the Co content, some CNTs appeared (Figures 1A and S1). The transmission electron microscopy (TEM) image of Co@NrC-0.3 reveals that many small metal nanoparticles with a mean diameter of ~16.1 nm were uniformly supported on the carbon framework and more importantly these particles were well capped by thin graphitic carbon layers (Figures 1B,D and S2). From the high-resolution (HR)-TEM images in Figure 1C,E,F, it was found that the outer carbon layers of marginal particles were not uniform, and almost all were less than 10 layers. Specifically, the majority of the carbon shells are one to seven layers thick. Such thin graphitic carbon layers are favorable for electron transport from the metal core to the carbon coat, so as to effectively enhance the catalytic behavior on the carbon shell.[27] Additionally, Figure 1G clearly shows that the lattice distance of the covered metal particle is 0.205 nm, which well corresponds to the (111) plane of the cubic metallic Co. Another distinct lattice fringe space of 0.35 nm in the carbon shell indicates the highly graphitic nature of the obtained material. The energy-dispersive X-ray (EDX) elemental mapping images are presented in Figure 1H, which verifies the uniform dispersion of Co, C, and N elements.

Figure 2A shows the corresponding X-ray diffraction (XRD) patterns of all obtained samples, which can further identify their composition. Similar diffraction features were detected in all samples. There are three obvious peaks at 44.03°, 51.30°, and 75.66°, exactly matching with the (111), (002), and (022) planes of cubic Co phases, respectively. As the amount of the Co raw materials increased, the diffraction peaks assigned to cubic Co became gradually stronger, revealing the existence of a larger proportion of metal Co. Besides, a remaining broad peak centered at ~26° can be indexed to C (002), which testifies the formation of graphene-like carbon. Such a result is in good agreement with the HRTEM observations. The accurate contents of Co metal in four Co@NrC hybrids are 13.07, 25.50, 37.15, and 48.09 wt%, respectively, based on inductively coupled plasma mass spectrometry (ICP-MS). In Raman spectra (Figure 2B), two typical peaks located at 1350 and 1583 cm^{-1} are observed, which represent the D and G bands, respectively. The graphitization degree on carbon materials is indicated by the G band while the strength of the D band suggests the structural defects in the carbon lattice.[28] By increasing the Co concentration of Co@NrC, the intensity ratio I_D/I_G decreased (Co@NrC-0.15: 1.01; Co@NrC-0.3: 0.99; Co@NrC-0.45: 0.93; Co@NrC-0.6: 0.91.) (Figure 2B), which implies that the incorporation of more metallic Co can reinforce the crystallinity of the carbon and reduce the quantity of the lattice defects. High graphitization degree is highly essential to good electrical conductivity while rich defect sites attribute to more active centers associated with oxygen electrocatalysis. Thereupon, to balance them, a moderate I_D/I_G value is required for the electrocatalytic process. The N_2 adsorption–desorption experiments of all samples were conducted out to disclose pore structure features and the surface area (SA). As can be seen from Figures 2C and S3, all Co@NrC hybrids have a typical type-IV isotherm with a hysteresis loop, indicating

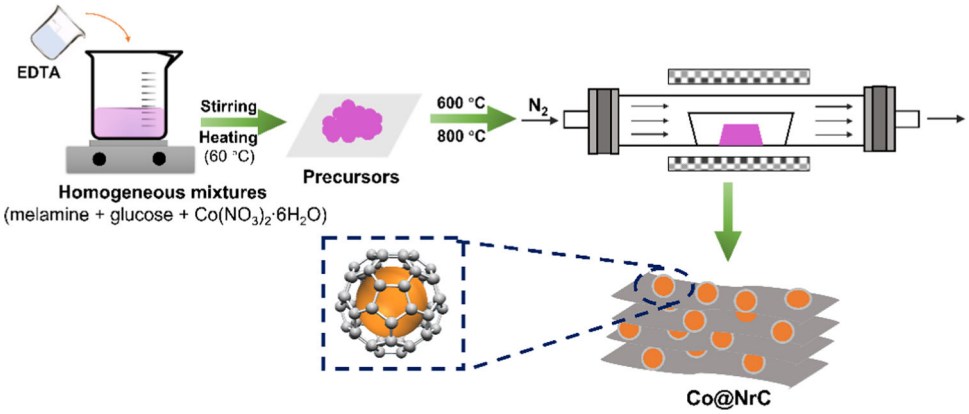

SCHEME 1 The schematic synthesis of the as-prepared Co@NrC samples

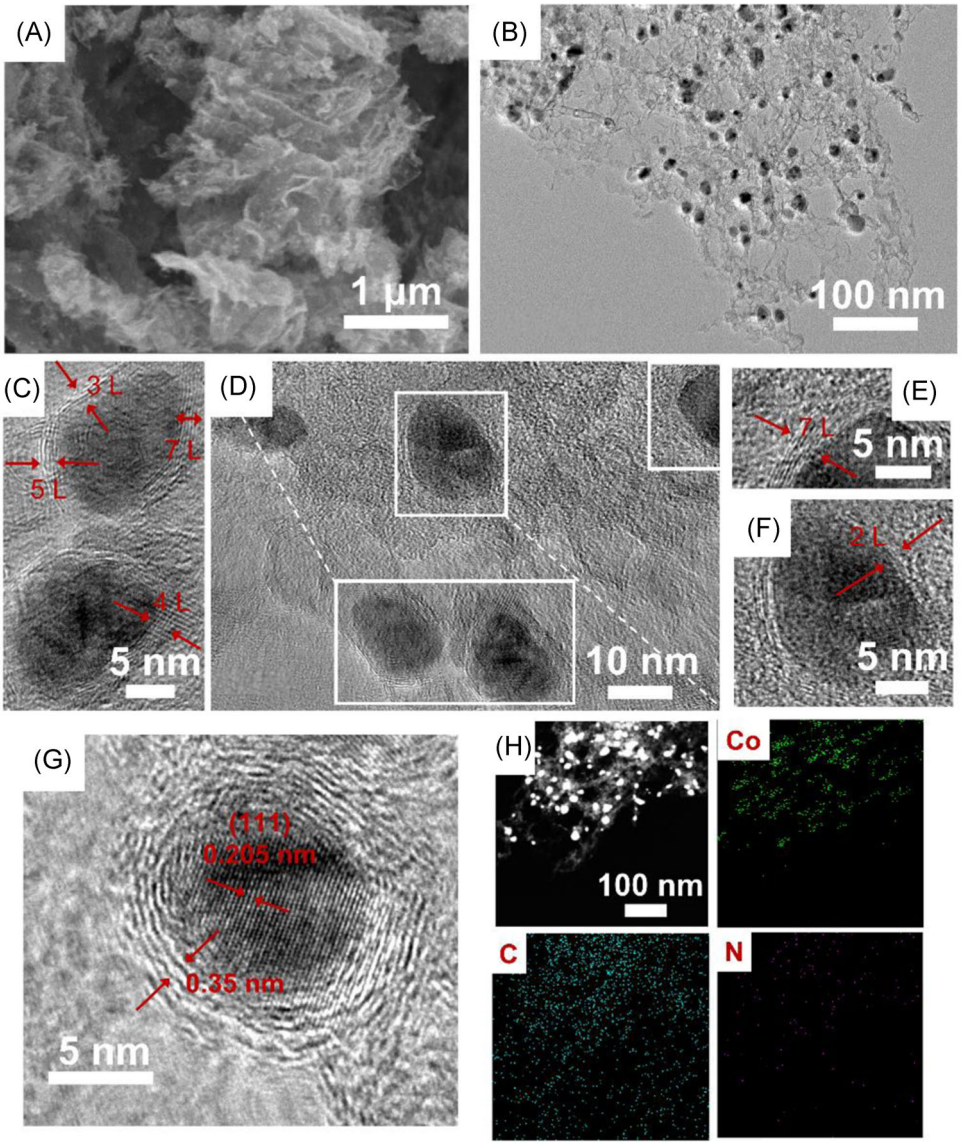

FIGURE 1 (A) SEM, (B) TEM, and (C-G) high-resolution TEM images of the Co@NrC-0.3 sample (L represents layers). (H) High-angle annular dark-field scanning transmission electron microscopy and the corresponding element mapping images of Co@NrC-0.3. SEM, scanning electron microscopy; TEM, transmission electron microscopy

similar mesoporous properties. Among the Co@NrC composites, Co@NrC-0.3 presented the largest specific SA of 273.6 $m^2 g^{-1}$. This large SA can be helpful to the electrocatalytic process in view of the availability of more catalytic active centers.

X-ray photoelectron spectroscopy (XPS) measurements were offered as a superb platform to observe the composition and valance state information of the Co@NrC samples. On basis of the full survey spectra (Figure S4), Co, N, and C elements were coexistent. Table S1 reveals that the nitrogen content determined by XPS declined with augmentation of the Co amount for the Co@NrC samples. The nitrogen concentration in Co@NrC-0.3 was 7.93 atom%. The high-resolution N 1s spectra in Figure 2D could be deconvoluted into five nitrogen species, that is, pyridinic N (398.4 eV), metal–N (399.3 eV), pyrrolic N (400.6 eV), graphitic N (401.9 eV), and oxidized N (404.8 eV), disclosing the successful doping of N.[29] Figures 2E and S5 depict the comparison of different N species in Co@NrC hybrids. The relative atom percentages of pyridinic N, metal–N, pyrrolic N, graphitic N, and oxidized N for Co@NrC-0.3 were calculated to be 33.10%, 21.71%, 21.62%, 15.20%, and 8.31%, respectively. As expected, the pyridinic N and metal–N ratios in Co@NrC-0.3 were larger than the results in other Co@NrC samples, which were deemed to play a vitally significant role in oxygen electrocatalysis, as reported in a previous study.[30,31] The deconvoluted

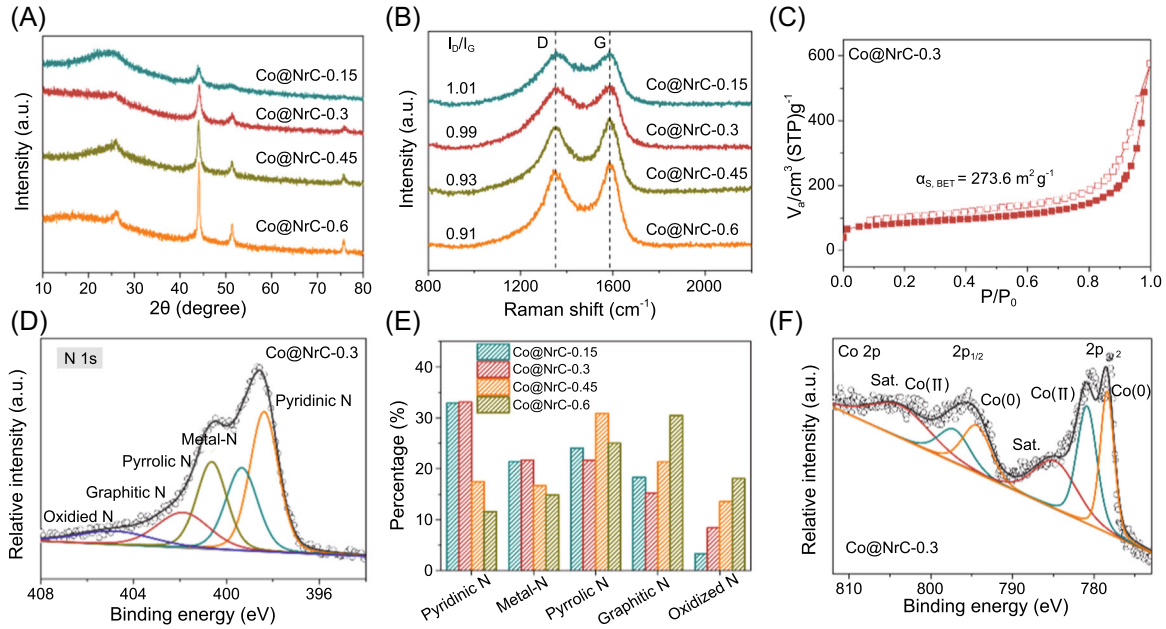

FIGURE 2 (A) XRD diffraction patterns and (B) Raman spectra of all Co@NrC samples. (C) N_2 adsorption/desorption isotherms and (D) high-resolution N 1s XPS spectrum of Co@NrC-0.3. (E) Relevant contents of various N species for all Co@NrC samples. (F) High-resolution Co 2p XPS spectrum of Co@NrC-0.3. XRD, X-ray diffraction; XPS, X-ray photoelectron spectroscopy

high-resolution C 1s spectra with four peaks of the C=C, C–N, C=N, and O=C–O bonds further substantiate the presence of the N dopants (Figure S6).[32] Besides, in the high-resolution Co 2p spectrum (Figure 2F and S7), two different chemical species of Co (0) and Co (II) were obtained. The Co (II) species was mainly due to the oxidation of Co metal.[33]

On basis of these abovementioned positive results, the ORR electrocatalytic behavior of all prepared Co@NrC hybrids and the commercial Pt/C were first evaluated in O_2-saturated 0.1 M KOH. All potentials were calibrated to a reversible hydrogen electrode (RHE). As described in Figure 3A, a clear ORR cathodic peak was observed in the cyclic voltammetry (CV) curve under the O_2-saturated KOH condition instead of N_2 atmosphere, demonstrating the electrocatalytic oxygen reduction ability of the Co@NrC-0.3 sample. Figure 3B presents the typical linear sweep voltammetry (LSV) curves of all materials. It is apparent that Co@NrC-0.3 had the higher onset and half-wave potentials ($E_{onset} = 0.97$ V; $E_{1/2} = 0.85$ V) than other Co@NrC catalysts (Co@NrC-0.15: $E_{onset} = 0.97$ V; $E_{1/2} = 0.85$ V; Co@NrC-0.45: $E_{onset} = 0.92$ V; $E_{1/2} = 0.81$ V; Co@NrC-0.6: $E_{onset} = 0.91$ V; $E_{1/2} = 0.81$ V), which was also comparable to the results of the benchmark Pt/C ($E_{onset} = 0.99$ V, $E_{1/2} = 0.85$ V). In addition, a large limiting current density of Co@NrC-0.3 further confirms the outstanding electrocatalytic activity. The Tafel slope plot of Co@NrC-0.3 in Figure 3C displays a value of 81 mV dec^{-1}. This value is not the lowest one among the results of Co@NrC, but it was also very close to that of Pt/C, suggesting a Pt-like ORR kinetic. As indicated by the Koutecky–Levich (K–L) data (Figure 3D), the electron transfer number for Co@NrC-0.3 was calculated to be about 3.8, representing a predominant four-electron process toward ORR. In addition to the ORR performance, the catalytic properties of these Co@NrC catalysts and commercial RuO_2 for OER were also investigated in 0.1 M KOH media. A small overpotential of 386 mV was needed to deliver the 10 mA cm^{-2} current density for the Co@NrC-0.3 sample, which is obviously better than other Co@NrC materials and commercial RuO_2 (Co@NrC-0.15: 466 mV; Co@NrC-0.45: 406 mV; Co@NrC-0.6: 407 mV; RuO_2: 440 mV) (Figure 3E). Besides, this Co@NrC-0.3 catalyst also offered a relatively small Tafel slope among all tested samples, which was 91 mV dec^{-1} (Figure 3F). This result signifies a good kinetic process of Co@NrC-0.3 for OER. The long-term durability is also critical for the commercialization of an electrocatalyst. The upper one in Figure 3G exhibits the ORR chronoamperometric response (i–t) of the optimal Co@NrC-0.3 and Pt/C samples at a fixed potential of 0.6 V. Obviously, the Co@NrC-0.3 hybrid manifested outstanding stability with a very minor loss (2%) of the initial current after a 12-h continuous operation, while an 18% loss was incurred for the benchmarked Pt/C. The large attenuation in Pt/C might be originated from the partial aggregation and detachment of Pt nanoparticles.[29]

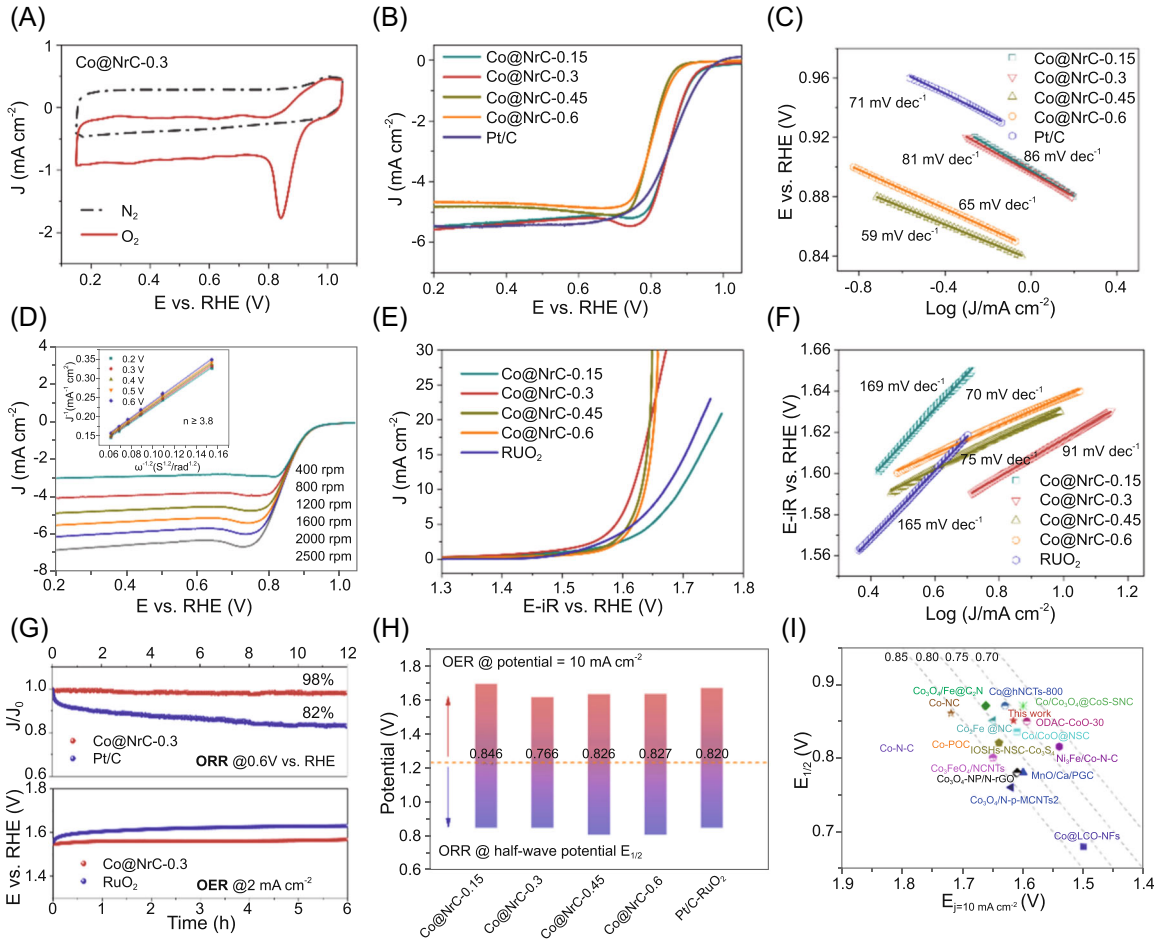

FIGURE 3 (A) The ORR CV curves of Co@NrC-0.3 in O_2- and N_2-saturated KOH solution. (B) LSV polarization curves and (C) the corresponding Tafel plots for ORR of all Co@NrC samples and Pt/C in 0.1 M KOH. (D) LSV curves at different rotation speeds and K–L plots of Co@NrC-0.3. (E) LSV polarization curves and (F) the corresponding Tafel plots for OER of all Co@NrC samples and RuO_2 in 0.1 M KOH. (G) ORR chronoamperometric response of the Co@NrC-0.3 and Pt/C samples at a fixed potential of 0.6 V and the OER chronopotentiometry testing of the Co@NrC-0.3 and RuO_2 samples at the current density of 2 mA cm^{-2}. (H) The potential gap (ΔE) between $E_j = 10$ mA cm^{-2} and $E_{1/2}$ of all Co@NrC samples and the Pt/C-RuO_2 couple. (I) The comparison of ΔE for our prepared Co@NrC-0.3 with reported Co-based bifunctional electrocatalysts. CV, cyclic voltammetry; K–L, Koutecky–Levich data; LSV, linear sweep voltammetry; OER, oxygen reduction reaction; ORR, oxygen evolution reaction

The OER durability of Co@NrC-0.3 and RuO_2 was also compared by conducting the chronopotentiometry testing at a current density of 2 mA cm^{-2} for 6 h (the below one in Figure 3G). The Co@NrC-0.3 catalyst clearly delivered a lower potential decay than that of RuO_2, suggesting a more stable feature of Co@NrC-0.3 during OER. In total, the above electrochemical results well reveal the excellent activity and stability of Co@NrC-0.3 as a bifunctional electrocatalyst for OER and ORR. As displayed in Figure 3H, the extraordinary bifunctionality of this Co@NrC-0.3 material for oxygen electrocatalytic reactions could be further assessed by calculating the ΔE value (the gap between the ORR half-wave potential [$E_{1/2}$] and OER potential at a current density of 10 mA cm^{-2} [$E_j = 10$ mA cm^{-2}]). The smallest ΔE value in the Co@NrC-0.3 catalyst ($\Delta E = 0.766$ V) was found among the comparative samples and noble metal materials. More importantly, such a result surpassed most of the reported Co-based bifunctional electrocatalysts (Figure 3I and Table S2).

Combining the aforementioned physical characterization and electrochemical data with the previous study, we also carried out some following control experiments and then systematically analyzed the origins of the extraordinary bifunctionality of the Co@NrC-0.3 catalyst. For sake of gaining deep insights into the effect of the encased Co, metal-free carbon with abundant N dopants (named as NrC) was further synthesized in absence of Co precursors. The NrC still showed a flake-like morphology (Figure S8) and had a high total N content and pyridinic N ratio according to XPS results (Table S1 and Figure S9). More significantly, its SA was also very large,

approximately 292.3 $m^2 g^{-1}$ (Figure S10). However, the ORR activity of NrC was obviously inferior to these of all Co@NrC catalysts (Figure S11). And as expected, a negligible OER activity was observed for NrC (Figure S11). Such findings well highlighted the importance of the implantation of cobalt in carbon materials for catalyzing the OER and ORR. Besides, it should be noted that Co single atoms are also likely embedded in the NrC scaffold, considering the synthesis method, which has been known to deliver active electrocatalytic activity toward OER and ORR in several previous studies.[34–36] To further determine the contribution from these single atoms on the OER and ORR performance, we subjected the Co@NrC-0.3 sample to etching for removing the metal–carbon core-shell structure; the resulting sample of which was named as s-Co@NrC. This is evident in the XRD patterns and HR-TEM images that show the absence of most Co nanoparticles (Figure S12A–C). According to the electrochemical measurement, s-Co@NrC indeed offered certain OER and ORR activities, which but was still largely inferior to the original Co@NrC-0.3 sample (Figure S12D,E). This suggests that the high performances of Co@NrC-0.3 mainly originated from the metal–carbon core-shell structure, instead of Co single atoms. Previous research works have demonstrated that the electrons from the metal core can be efficiently transferred to the thin carbon shell in the core-shell-structured metal–carbon composites owing to their intimate contact, and as such, this carbon layer became more active toward the O_2 adsorption and dissociation and eventually promoted the OER and ORR processes.[33] Specifically, as elucidated by XPS, there was a prominent energy shifting triggered by the strong electron interactions between some implanted metal atoms and pyrrolic N species of the carbon skeleton, which brought about the appearance of the metal–N bond. Meanwhile, the abundant N-related functional groups (especially pyridinic N and metal–N) in carbon materials feature with the strong electron-withdrawing capability, which could induce more charge on the nearby C atoms and thereby bestow them as active sites toward oxygen electrocatalysis.[23,27] Among the various Co@NrC materials with different Co content, Co@NrC-0.3 held the best metal–carbon core-shell structure for ORR and OER due to the largest specific area, optimal carbon structure (sufficient conductivity and a certain amount of defect sites), and high pyridinic N and metal–N ratios. Besides, a larger electrochemical active surface area (ECSA) was found in the Co@NrC-0.3 material in comparison with other Co@NrC samples (Figure S13), which reveals a better exposure and improved utilization of active sites. As to the morphological structure–activity relationship, it was believed that the highly interconnected porous graphitic carbon framework with a large specific SA for Co@NrC-0.3 was favorable to excellent charge (ions and electrons) transport in the electrocatalysis process, which helped to catalyze ORR and OER. Simultaneously, the continuous carbon layer prevented the inner metal from the undesired detachment and agglomeration, so as to ensure robust structural stability under long-life operation conditions. To further elucidate this relationship, the Co@NrC-0.3 catalyst was ball-milled for 3 h to destroy the interconnected porous structure with a large SA and Co@NrC-0.3-d was attained. The Co@NrC-0.3-d presented a relatively low SA when compared to that of Co@NrC-0.3 (Figure S14). As expected, this contrast sample (Co@NrC-0.3-d) exhibited unsatisfied ORR and OER activities relative to Co@NrC-0.3 (Figure S15).

The splendid bifunctionality toward OER and ORR in the alkaline electrolyte endowed the Co@NrC-0.3 material with a promising application potential as a cathode catalyst in a homemade ZAB. Consequently, the aqueous ZAB was assembled with Zn foil as the anodic electrode, the carbon paper supported Co@NrC-0.3 as the air electrode, and the 6 M KOH + 0.2 M $Zn(Ac)_2$ solution as the electrolyte, as illustrated in Figure S16. For comparison, the benchmark Pt/C-RuO_2 couple was tested in another battery. The Co@NrC-0.3-based ZAB offered a larger open-circuit voltage (OCV) of 1.47 V than that of the Pt/C + RuO_2-based ZAB (1.44 V) (Figure 4A). The polarization curves in Figure 4B manifest that the higher discharge voltages of 1.32, 1.19, and 1.05 V at the current densities of 10, 50, and 100 mA cm^{-2} were attained in Co@NrC-0.3-based ZAB in comparison with the battery with the Pt/C-RuO_2 catalyst (its discharge voltages were 1.28, 1.13, and 0.98 V at the current densities of 10, 50, and 100 mA cm^{-2}). Moreover, the peak power density of this Co@NrC-0.3-based battery was as high as 168 mW cm^{-2} (Figure 4C), which clearly outperformed that of the Pt/C + RuO_2-based battery (151 mW cm^{-2}) and also was competitive to many recently reported results (Table S3). As shown in Figure 4C, A small discharge-charge potential gap of 0.45 V at 10 mA cm^{-2} for the battery with the Co@NrC-0.3 catalyst indicates efficient reversibility of this rechargeable ZAB. Such a small potential gap at the initial stage could be derived from the Co oxidation.[37,38] Figure 4D presents discharge rate performance curves of Co@NrC-0.3 at various current densities from 1 to 50 mA cm^{-2}. The discharge potential decreased with the increase of the current density, and the potential could well recover with inconspicuous fading when the current density was restored to the original state. Such finding signifies that Co@NrC-0.3 had a good rate performance and superior reversibility. The long-term cyclability of the assembled Co@NrC-0.3-based ZAB was further investigated at 2 mA cm^{-2} (Figure 4E). Notably, in the initial cycle, the battery with Co@NrC-0.3 showed a small initial charge-discharge overpotential. However, after

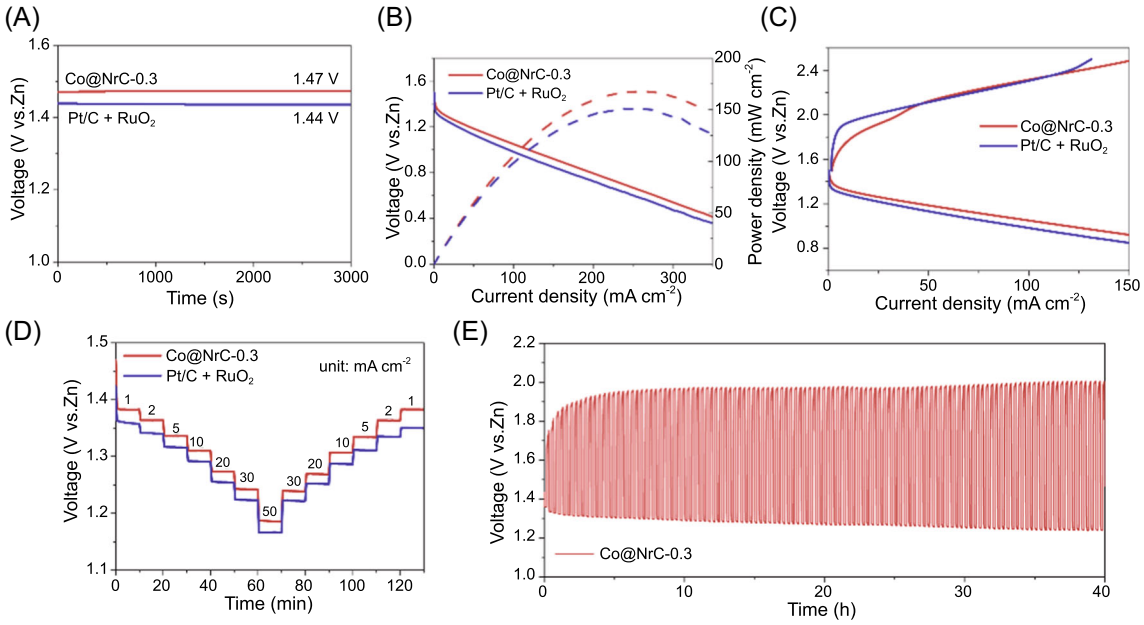

FIGURE 4 (A) The open-circuit voltage plots, (B) the discharge polarization curves and the corresponding power density, (C) discharge-charge polarization curves, and (D) discharge rate performance curves at various current densities of the fabricated aqueous ZABs with Co@NrC-0.3 or Pt/C + RuO_2. (E) The long-term discharge–charge cyclability curve of the Co@NrC-0.3-based ZAB at a current density of 2 mA cm^{-2}. ZAB, zinc-air battery

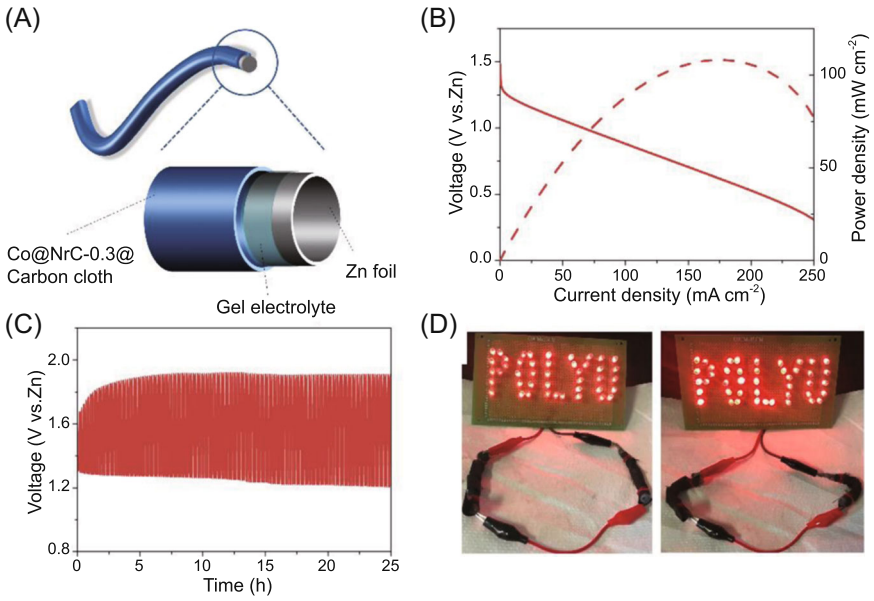

FIGURE 5 (A) Schematic illustration displaying the flexible all-solid-state ZAB. (B) The discharge polarization curve and the corresponding power density, and (C) the long-term discharge–charge cycle stability at a current density of 1 mA cm^{-2} of the Co@NrC-0.3-based ZAB. (D) LED lights powered by two flexible solid-state ZABs under normal and bending conditions. ZAB, zinc-air battery; LED, light emitting diode

40 h (about 120 cycles), some performance losses, such as the increased voltage gap, were found. The relatively insufficient stability for Co@NrC-0.3 might be originated from the initial Co oxidation contribution and subsequent carbon oxidation corrosion during the OER process.[37,38]

Given the booming demand for flexible electronic devices, the Co@NrC-0.3 was further applied into the flexible all-solid-state ZAB for expanding its practical application. In this solid-state battery, supple zinc foil was used as the anode, the alkaline gel polymer gel

(KOH + polyacrylic acid) was employed as the solid electrolyte, and the carbon cloth coated with Co@NrC-0.3 was used as the cathode (Figure 5A). The constructed Co@NrC-0.3-based solid-state battery delivered a high OCV of 1.40 V (Figure S17). The peak power density of this ZAB with Co@NrC-0.3 was determined to be 108 mW cm^{-2} at 174 mA cm^{-2} (Figure 5B), which surpassed most of the previous solid-state ZABs (Table S4). As depicted in Figure 5C, the galvanostatic discharge–charge cycle measurement at 1 mA cm^{-2} showed a continuous and steady 15 h operation, disclosing the relatively good stability of the Co@NrC-0.3-based solid-state battery. As a demonstration, some LED (light emitting diode) lights composing the words of "POLYU" were powered by two Co@NrC-0.3-based solid-state ZABs connected in series (Figure 5D). More impressively, these ZABs under bending conditions also can successfully light these LEDs (Figure 5D), which suggests excellent flexibility.

3 | CONCLUSION

In summary, a composite of Co nanoparticles embedded in N-rich graphitic carbon layers was successfully fabricated by a facile mixing-calcination method. The resulting Co@NrC-0.3 catalyst with optimal Co concentration not only demonstrated excellent OER and HER catalytic activity in alkaline electrolyte with the ΔE of 0.766 V but also exhibited prominent long-life stability. These outstanding catalytic properties could be attributed to the unique core-shell structure with the good optimization of oxygen adsorption/dissociation ability. More encouragingly, when applied to the rechargeable liquid ZAB, the battery with Co@NrC-0.3 displayed a high maximum power density of 168 mW cm^{-2}, a small initial discharge–charge potential gap of 0.45 V at 10 mA cm^{-2}, and superior rate performance. Moreover, a prominent potential application in this flexible all-solid-state ZAB was attained for this catalyst. These results indicate an effective strategy to rationally develop and construct the high-activity and low-cost bifunctional electrocatalysts for the promising ZAB devices.

ACKNOWLEDGMENTS

This study is supported by a grant under the Theme-based Scheme (project number: T23-601/17-R) from Research Grant Council, University Grants Committee, Hong Kong SAR, China.

CONFLICT OF INTEREST

The authors declare no conflict of interest.

REFERENCES

1. Sun W, Wang F, Zhang B, et al. A rechargeable zinc-air battery based on zinc peroxide chemistry. *Science*. 2021;371(6524):46-51.
2. Sumboja A, Liu J, Zheng WG, Zong Y, Zhang H, Liu Z. Electrochemical energy storage devices for wearable technology: a rationale for materials selection and cell design. *Chem Soc Rev*. 2018;47(15):5919-5945.
3. Pan J, Xu YY, Yang H, Dong Z, Liu H, Xia BY. Advanced architectures and relatives of air electrodes in Zn–air batteries. *Adv Sci*. 2018;5(4):1700691.
4. Tan P, Chen B, Xu H, et al. Flexible Zn- and Li-air batteries: recent advances, challenges, and future perspectives. *Energy Environ Sci*. 2017;10(10):2056-2080.
5. Dai Y, Yu J, Cheng C, Tan P, Ni M. Mini-review of perovskite oxides as oxygen electrocatalysts for rechargeable zinc-air batteries. *Chem Eng J*. 2020;397:125516.
6. Wang HF, Tang C, Zhang Q. A review of precious-metal-free bifunctional oxygen electrocatalysts: rational design and applications in Zn-air batteries. *Adv Funct Mater*. 2018;28(46):1803329.
7. Tian X, Zhao X, Su Y-Q, et al. Engineering bunched Pt-Ni alloy nanocages for efficient oxygen reduction in practical fuel cells. *Science*. 2019;366(6467):850-856.
8. Yu J, He Q, Yang G, Zhou W, Shao Z, Ni M. Recent advances and prospective in ruthenium-based materials for electrochemical water splitting. *ACS Catal*. 2019;9(11):9973-10011.
9. Yu J, Ran R, Zhong Y, Zhou W, Ni M, Shao Z. Advances in porous perovskites: synthesis and electrocatalytic performance in fuel cells and metal-air batteries. *Energy Environ Mater*. 2020;3(2):121-145.
10. Lu Q, Yu J, Zou X, et al. Self-catalyzed growth of Co, N-codoped CNTs on carbon-encased CoS_x surface: a noble-metal-free bifunctional oxygen electrocatalyst for flexible solid Zn-air batteries. *Adv Funct Mater*. 2019;29(38):1904481.
11. Zhou T, Zhang N, Wu C, Xie Y. Surface/interface nanoengineering for rechargeable Zn-air batteries. *Energy Environ Sci*. 2020;13(4):1132-1153.
12. Yan X, Jia Y, Yao X. Defects on carbons for electrocatalytic oxygen reduction. *Chem Soc Rev*. 2018;47(20):7628-7658.
13. Zhou Y, Chen G, Zhang J. A review of advanced metal-free carbon catalysts for oxygen reduction reactions towards the selective generation of hydrogen peroxide. *J Mater Chem A*. 2020;8(40):20849-20869.
14. Wang Z, Li Q-K, Zhang C, et al. Hydrogen peroxide generation with 100% Faradaic efficiency on metal-free carbon black. *ACS Catal*. 2021;11(4):2454-2459.
15. Wei W, Liang H, Parvez K, Zhuang X, Feng X, Müllen K. Nitrogen-doped carbon nanosheets with size-defined mesopores as highly efficient metal-free catalyst for the oxygen reduction reaction. *Angew Chem Int Ed*. 2014;126(6):1596-1600.
16. Sun J, Lowe SE, Zhang L, et al. Ultrathin nitrogen-doped holey carbon@graphene bifunctional electrocatalyst for oxygen reduction and evolution reactions in alkaline and acidic media. *Angew Chem Int Ed*. 2018;57(50):16511-16515.
17. Yu J, Sunarso J, Zhuang W, et al. Synthesis of highly porous metal-free oxygen reduction electrocatalysts in a self-sacrificial bacterial cellulose microreactor. *Adv Sustainable Syst*. 2017;1(7):1700045.

18. Zhang J, Zhao Z, Xia Z, Dai L. A metal-free bifunctional electrocatalyst for oxygen reduction and oxygen evolution reactions. *Nat Nanotechnol*. 2015;10(5):444-452.
19. Zhang Y, Fan X, Jian J, Yu D, Zhang Z, Dai L. A general polymer-assisted strategy enables unexpected efficient metal-free oxygen-evolution catalysis on pure carbon nanotubes. *Energy Environ Sci*. 2017;10(11):2312-2317.
20. Cheng N, Liu Q, Tian J, et al. Acidically oxidized carbon cloth: a novel metal-free oxygen evolution electrode with high catalytic activity. *Chem Commun*. 2015;51(9):1616-1619.
21. Yu J, Chen G, Sunarso J, et al. Cobalt oxide and cobalt-graphitic carbon core-shell based catalysts with remarkably high oxygen reduction reaction activity. *Adv Sci*. 2016;3(9):1600060.
22. Singh SK, Takeyasu K, Nakamura J. Active sites and mechanism of oxygen reduction reaction electrocatalysis on nitrogen-doped carbon materials. *Adv Mater*. 2019;31(13):1804297.
23. Jiang P, Chen J, Wang C, et al. Tuning the activity of carbon for electrocatalytic hydrogen evolution via an iridium-cobalt alloy core encapsulated in nitrogen-doped carbon cages. *Adv Mater*. 2018;30(9):1705324.
24. Zhang J, Dai L. Nitrogen, phosphorus, and fluorine tri-doped graphene as a multifunctional catalyst for self-powered electrochemical water splitting. *Angew Chem Int Ed*. 2016;55(42):13296-13300.
25. Deng D, Yu L, Chen X, et al. Iron encapsulated within pod-like carbon nanotubes for oxygen reduction reaction. *Angew Chem Int Ed*. 2013;125(1):389-393.
26. Yu L, Deng D, Bao X. Chain mail for catalysts. *Angew Chem Int Ed*. 2020;59(36):15294-15297.
27. Su J, Yang Y, Xia G, Chen J, Jiang P, Chen Q. Ruthenium-cobalt nanoalloys encapsulated in nitrogen-doped graphene as active electrocatalysts for producing hydrogen in alkaline media. *Nat Commun*. 2017;8:1-12.
28. Yu J, Guo Y, Miao S, Ni M, Zhou W, Shao Z. Spherical ruthenium disulfide-sulfur-doped graphene composite as an efficient hydrogen evolution electrocatalyst. *ACS Appl Mater Interfaces*. 2018;10(40):34098-34107.
29. Xu Y, Deng P, Chen G, et al. 2D nitrogen-doped carbon nanotubes/graphene hybrid as bifunctional oxygen electrocatalyst for long-life rechargeable Zn-air batteries. *Adv Funct Mater*. 2020;30(6):1906081.
30. Wang Z, Lu Y, Yan Y, et al. Core-shell carbon materials derived from metal-organic frameworks as an efficient oxygen bifunctional electrocatalyst. *Nano Energy*. 2016;30:368-378.
31. Xia BY, Yan Y, Li N, Wu HB, Lou XW, Wang X. A metal-organic framework-derived bifunctional oxygen electrocatalyst. *Nat Energy*. 2016;1(1):15006.
32. Hao X, Jiang Z, Zhang B, et al. N-doped carbon nanotubes derived from graphene oxide with embedment of FeCo nanoparticles as bifunctional air electrode for rechargeable liquid and flexible all-solid-state zinc-air batteries. *Adv Sci*. 2021;8(10):2004572.
33. Rao P, Liu Y, Su Y-Q, et al. S, N co-doped carbon nanotube encased Co NPs as efficient bifunctional oxygen electrocatalysts for zinc-air batteries. *Chem Eng J*. 2021;422:130135.
34. Sun X, Sun S, Gu S, et al. High-performance single atom bifunctional oxygen catalysts derived from ZIF-67 superstructures. *Nano Energy*. 2019;61:245-250.
35. Xie W, Song Y, Li S, et al. Single-atomic-Co electrocatalysts with self-supported architecture toward oxygen-involved reaction. *Adv Funct Mater*. 2019;29(50):1906477.
36. Tavakkoli M, Flahaut E, Peljo P, et al. Mesoporous single-atom-doped graphene-carbon nanotube hybrid: synthesis and tunable electrocatalytic activity for oxygen evolution and reduction reactions. *ACS Catal*. 2020;10(8):4647-4658.
37. Pan L, Chen D, Pei P, Huang S, Ren P, Song X. A novel structural design of air cathodes expanding three-phase reaction interfaces for zinc-air batteries. *Appl Energy*. 2021;290(15):116777.
38. Tan P, Chen B, Xu H, Cai W, He W, Ni M. In-situ growth of Co_3O_4 nanowire-assembled clusters on nickel foam for aqueous rechargeable Zn-Co_3O_4 and Zn-air batteries. *Appl Catal B*. 2019;241:104-112.

SUPPORTING INFORMATION

Additional supporting information may be found in the online version of the article at the publisher's website.

How to cite this article: Yu J, Dai Y, Zhang Z, et al. Tailoring structural properties of carbon via implanting optimal Co nanoparticles in N-rich carbon cages toward high-efficiency oxygen electrocatalysis for rechargeable Zn-air batteries. *Carbon Energy*. 2022;4:576-585. doi:10.1002/cey2.171